Ligand Coupling Symmetry Correlates with Thermopower Enhancement in Small-Molecule/Nanocrystal Hybrid Materials

Jared Lynch,[†] Michele Kotiuga,[†,‡] Vicky V. T. Doan-Nguyen,[⊥] Wendy L. Queen,[†] Jason D. Forster,[†] Ruth A. Schlitz,[∥] Christopher B. Murray,[§,⊥] Jeffrey B. Neaton,[†,‡,¶] Michael L. Chabinyc,[∥] and Jeffrey J. Urban*[,†]

[†]Materials Science Division, The Molecular Foundry, Lawrence Berkeley National Laboratory, One Cyclotron Road, Berkeley, California 94720, United States, [‡]Department of Physics, University of California, Berkeley, California 94720-7300, United States, [§]Department of Chemistry and [⊥]Department of Materials Sciences and Engineering, University of Pennsylvania, Philadelphia, Pennsylvania 19104, United States, [¶]Kavli Energy NanoSciences Institute at Berkeley, Berkeley, California, United States, and [∥]Materials Department, University of California, Santa Barbara, California 93106-6105, United States

ABSTRACT We investigate the impact of the coupling symmetry and chemical nature of organic–inorganic interfaces on thermoelectric transport in $Cu_{2-x}Se$ nanocrystal thin films. By coupling ligand-exchange techniques with layer-by-layer assembly methods, we are able to systematically vary nanocrystal–organic linker interfaces, demonstrating how the functionality of the polar headgroup and the coupling symmetry of the organic linkers can change the power factor ($S^2\sigma$) by nearly 2 orders of magnitude. Remarkably, we observe that ligand-coupling symmetry has a profound effect on thermoelectric transport in these hybrid materials. We shed light on these results using intuition from a simplified model for interparticle charge transport *via* tunneling through the frontier orbital of a bound ligand. Our analysis indicates that ligand-coupling symmetry and binding mechanisms correlate with enhanced conductivity approaching 2000 S/cm, and we employ this concept to demonstrate among the highest power factors measured for quantum-dot based thermoelectric inorganic–organic composite materials of ~30 μW/m·K^2.

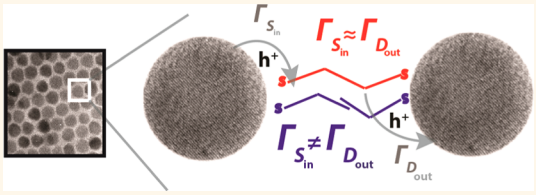

KEYWORDS: thermoelectrics · coupling · ligand exchange · copper selenide · nanocrystal · composite · hybrid · organic

Recently, nanocrystalline-based thermoelectric materials have garnered increased attention as low cost, scalable alternatives to commercially grown inorganic thin films.[1−4] Colloidal inorganic nanocrystals are promising candidates for use as the next generation of thermoelectric materials because their dimensions approach the fundamental length scales of charge and heat transport and the accessibility of tuning crystal sizes and band gaps using synthetic means. In addition, the fact that these materials are solution-processed opens up new avenues in thermoelectrics, including compatibility with flexible substrates.[3,5]

The figure of merit used to evaluate the performance of thermoelectric materials is given by

$$ZT = \frac{S^2\sigma T}{k} \qquad (1)$$

where S is the Seebeck coefficient (or thermopower), σ is the electrical conductivity, k is the thermal conductivity, and T is the temperature. Introducing nanointerfaces into traditionally grown thermoelectric materials has been demonstrated to improve ZT, primarily by reducing the thermal conductivity of the parent material, attributed to enhanced phonon scattering at the boundaries of the nanostructures.[6,7] In contrast, relatively little work involving nanocrystalline thermoelectrics has involved enhancing the power factor ($S^2\sigma$). Intriguingly, hybrid organic–inorganic systems offer the ability to take advantage of the complementary interactions between these two materials to dramatically enhance the power factor.[8−10] Model calculations indicate that proper tuning of electronic energy levels and nanocrystal couplings in these hybrid organic–inorganic systems can yield ZT values well in excess of 30.[11] Our goal is to take advantage of the unique attributes that both organic and inorganic components offer in a new form of hybrid nanocrystal

* Address correspondence to jjurban@lbl.gov.

Received for review July 18, 2014 and accepted September 11, 2014.

Published online September 11, 2014
10.1021/nn503972v

composite. To date, despite the potential of these hybrid inorganic−organic materials, at present they have not achieved high performance, with thermopowers that typically range around 1−5 μW/m·K^2.[5,12] Thus, there is clearly a need for a more fundamental and comprehensive understanding of the direct role that inorganic−organic interfaces have on transport properties in nanocrystal composites.

Currently, the precise physical and chemical nature of heterointerfaces at the nanoscale is poorly understood and challenging to chemically control and manipulate. In this paper, we study the effect of molecular interfaces and organic−inorganic binding in composites by preparing simplified systems in which the thin-film behavior can be understood as manifesting the behavior of a collection of molecular-scale junctions between nanocrystals. Single molecule STM break junction studies of such interfaces on gold films have shown that the functionality of the binding polar headgroup and the conjugation of the organic molecule's backbone can strongly affect the measured conductance and thermopower across the inorganic−organic interface.[9,10] Further studies confirmed the importance of several key properties of the organic component, such as energy levels, molecular length, and backbone aromaticity that strongly influence thermoelectric transport through molecular junctions.[13−15] Despite these insights, single molecule studies on thermoelectric properties have thus far largely focused on symmetric, bifunctional molecules with two surface-binding functionalities on each end, allowing direct bonding between the substrate surface and the STM tip.[16] Thus, the effects of the junction's cross-linking symmetry on transport properties have yet to be fully elucidated at the atomic level, in part due to the difficulty of executing those measurements with molecules that do not strongly bind to both tip and surface. Fundamentally, however, the asymmetry present in nonsymmetric, monofunctinal molecules has the potential to introduce vectorial barriers to transport of the type that are known to enhance thermopower in thermionic and carrier-filtering schemes.[17,18] Understanding how these molecular properties apply when there are exponentially greater numbers of molecular junctions, such as in nanocrystal composites, will be critical for optimizing nanocrystal based devices.

Here, we use layer-by-layer deposition methods for both organic and inorganic components to make assemblies with well-controlled interfaces allowing for different small molecules to be introduced homogeneously throughout the film. Developing a theoretical framework to understand the trends which emerge from changes in the chemistry and coupling symmetry of the organic linkers used is essential, as these new materials conform to neither bandlike transport models for inorganic materials nor purely variable-range hopping models for disordered molecular organics. These systems demonstrate global incoherent transport, yet locally, we expect coherent tunneling *via* ligands between neighboring nanoparticles in the film.

We focus on copper chalcogenide nanocrystals connected by small molecule organic species. Copper chalcogenides are an appealing materials system for thermoelectric applications due to their intrinsically low thermal conductivities, high thermopowers, and interesting and complex phase transition behavior.[19,20] In bulk films, $Cu_{2-x}Se$ has conductivities up to 10^5 $\Omega^{-1}m^{-1}$ with surprisingly low thermal conductivities less than 1 W/m·K.[20] Moreover, copper selenide is well suited to match with the ionization potentials and electron affinities of a wide variety of organic molecules relevant to hybrid thermoelectric materials, with a valence band energy level estimated at −4.7 eV relative to vacuum and direct and indirect bandgaps of ∼2.2 and ∼1.2 eV, respectively.[20,21] In nanocrystalline form, copper chalcogenides can undergo p-type doping by simple exposure to air leading to the nonstoichiometric molecular composition $Cu_{2-x}B$ (B = S, Se, Te) where x typically ranges from 0.2 to 0.3.[22] This vacancy, p-type self-doping occurs through oxidation of Cu^{1+} to Cu^{2+} leaving behind a free hole which, in nanocrystals, leads to the formation of a broadband localized surface plasmon (LSP) absorption in the near-infrared.[23] These LSPs have been theoretically modeled as a function of the nanocrystal size and distribution to better understand how such criteria affects the shape and intensity of the absorption profiles in solution and on film.[23,24]

RESULTS AND DISCUSSION

$Cu_{2-x}Se$ nanocrystals were prepared using a solution-based colloidal synthesis in which a Cu−oleylamine complex was injected at elevated temperature into a Se−oleylamine complex. The resulting 13.5 ± 1.0 nm nanocrystals had narrow size distribution and could be well dispersed in nonpolar solvents for use in thin film assembly (Figure 1a). The as-prepared $Cu_{2-x}Se$ nanocrystals show a broad LSP band in the NIR signifying Cu vacancy doping as previously reported (Figure 1c).[22] The XRD of the $Cu_{2-x}Se$ nanocrystals shows characteristic peaks indicative of the cubic crystal phase of nonstoichiometric copper selenide (Figure 1d). Dip-coating and solution-phase ligand-exchange procedures were used to prepare nanocrystal assemblies with a series of small, symmetric, bifunctional ligands having the same binding group on both ends of the carbon backbone along with asymmetric, monofunctional organic molecules with a corresponding binding group on one end and a methyl group on the other to determine the effect of different inorganic−organic interfaces on the transport properties of the $Cu_{2-x}Se$ nanocrystal thin films (Figure 1b). Throughout the remainder of the text, we shall define bifunctional ligands with two similar polar surface binding groups

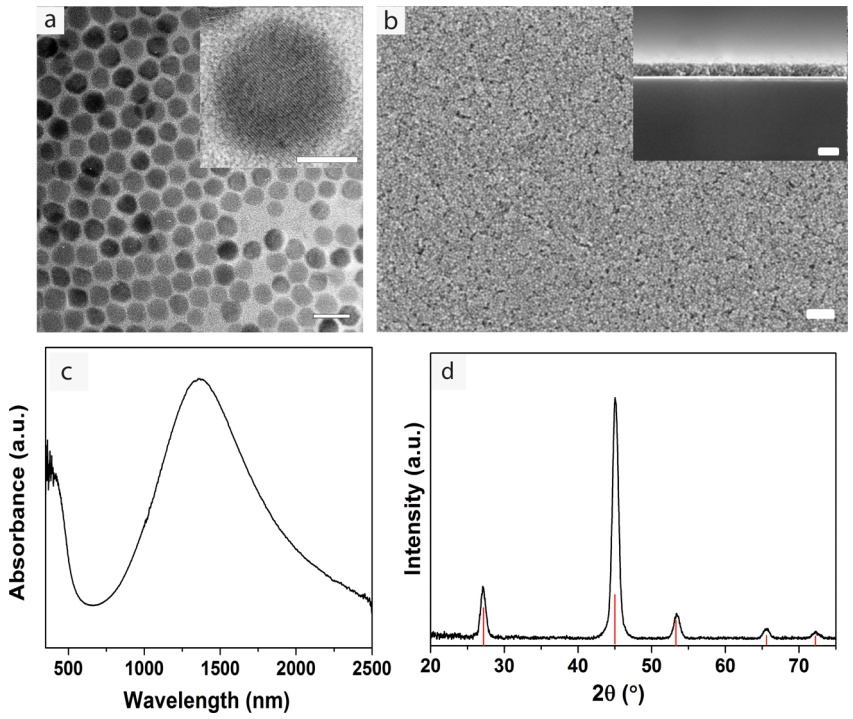

Figure 1. (a) TEM image of 13.5 ± 1.0 nm $Cu_{2-x}Se$ nanocrystals used for thin film preparation, 50 nm scale bar; (inset) high resolution TEM image of a $Cu_{2-x}Se$ nanocrystal, 5 nm scale bar. (b) Top view SEM image of representative $Cu_{2-x}Se$ nanocrystal thin film; (inset) side view of same film, 100 nm scale bars. (c) Absorption spectra of $Cu_{2-x}Se$ nanocrystals in TCE solution. (d) XRD spectra of $Cu_{2-x}Se$ nanocrystals, showing reference peak (01-088-2043 (*), berzelianite; syn, Cu_2Se).

as having the ability to "symmetrically" cross-link two neighboring nanocrystals; likewise, the monofunctional ligands with one polar surface binding group and a nonsurface interacting methyl group can only form asymmetrical junctions where no cross-linking can occur. When referring to these two types of ligands and the junctions they form between nanocrystals, we shall use "symmetric" and "asymmetric" from now on. Films were prepared on cleaned glass substrates using a layer-by-layer assembly process allowing for fine control of film thicknesses ranging from 65 to 200 nm (Figure 1b). For 65−80 nm thick films, gold top contacts were evaporated on the $Cu_{2-x}Se$ nanocrystal thin films, and then the Seebeck coefficient and electrical conductivity were measured. All $Cu_{2-x}Se$ nanocrystal thin film samples were prepared and measured inside nitrogen-filled gloveboxes. We keep the inorganic $Cu_{2-x}Se$ nanocrystals and their spacing near constant, allowing exploration of both energy level alignment and asymmetrical electronic coupling effects. We use a range of organic ligands of comparable length but with different binding groups and polarities. Furthermore, we use both single and dibinding ligands of commonly used surface binding groups: amines, thiols, and carboxylic acids. We also use a common ligand stripping procedure to produce a bare "ligand free" surface.[25] Assuming complete ligand stripping and thorough rinsing of excess reagents and ligands, the stripping can be used as an internal control acting as a system with the shortest possible interparticle spacing between two neighboring nanocrystals. In most nanocrystal syntheses to date, these chemical functionalities have been crucial to obtaining the desired size, distribution, shapes, and solubility of inorganic nanoparticles.

To ensure consistent interparticle spacing, we chose small organic ligands with similar structural backbones (two repeating CH_2 units) but different polar binding head groups. IR spectroscopy was used to monitor ligand exchange efficiency.[26−28] The IR spectra of ~200 nm thick $Cu_{2-x}Se$ films were measured, and the intensity of the C−H stretch centered near 2900 cm^{-1} was compared before and after ligand exchange (Figure 2a,c). The expected decrease in the C−H stretch intensity was consistent for all of the small organic ligands used. The asymmetric ligands show larger residual C−H stretching regions due to the greater amount of C−H repeating units in the asymmetric versus the symmetric. We captured scanning electron microscopy (SEM) images for each film prepared using dip coating layer-by-layer assembly. SEM analysis of the nanocrystal composites with symmetric (Figure 3) and asymmetric (Figure S1, Supporting Information) ligands clearly show all of the nanocrystal thin films are randomly packed with no observable cracks or other physical distortions that might affect carrier transport. Overall, IR and SEM analysis support our hypothesis; by keeping interparticle spacing constant and conserving the random order and quality between all of the films studied, we are able to isolate

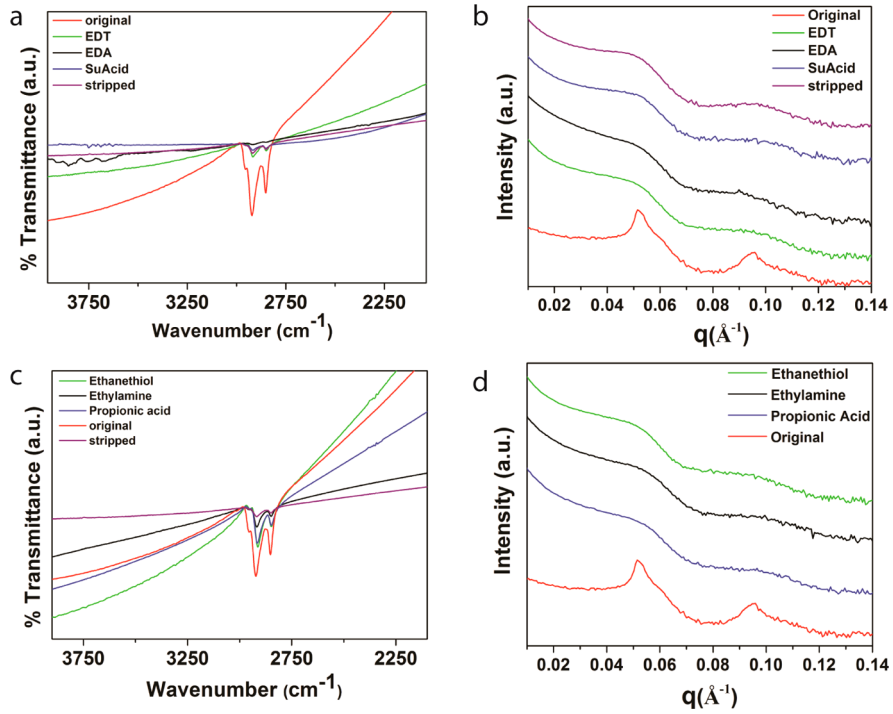

Figure 2. (a) Zoom in of normalized FTIR spectra in the C−H stretch region of $Cu_{2-x}Se$ nanocrystal thin films with different symmetric ligands. (b) GISAXS spectra of $Cu_{2-x}Se$ nanocrystal thin films with different symmetric ligands. (c) Zoom in of normalized FTIR spectra in the C−H stretch region of $Cu_{2-x}Se$ nanocrystal thin films with different asymmetric ligands. (d) GISAXS spectra of $Cu_{2-x}Se$ nanocrystal thin films with different asymmetric ligands.

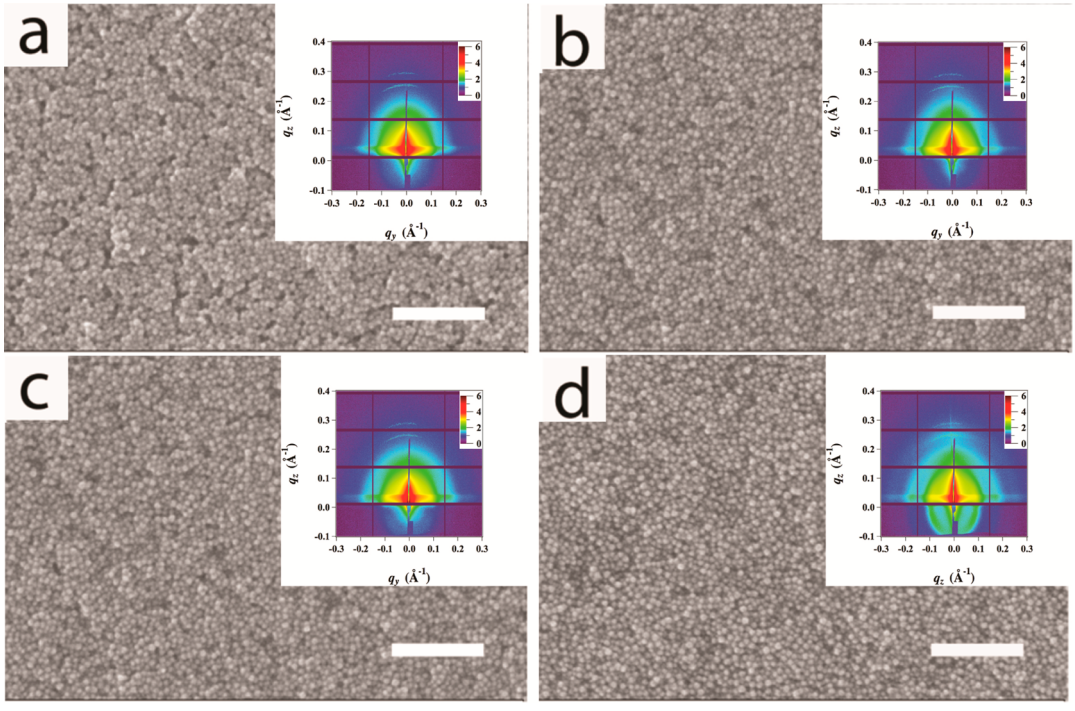

Figure 3. SEM images of $Cu_{2-x}Se$ nanocrystal thin film with different symmetric ligands: (a) ethylenediamine, (b) succinic acid, (c) 1,2 ethanedithiol, (d) stripped. (Inset) GISAXS patterns with line cuts showing loss of long-range order. All scale bars are 200 nm.

and probe the effects of ligand chemistry and coupling symmetry.

To confirm that the average interparticle spacing between $Cu_{2-x}Se$ nanocrystals was similar for all of the organic ligands used and that the periodicity/packing were not responsible for the measured differences in conductivity and Seebeck coefficient, GISAXS measurements were performed on $Cu_{2-x}Se$ films with each

symmetric and asymmetric ligand (Figure 2b,d). The GISAXS measurement for a drop cast film of the as-made $Cu_{2-x}Se$ nanocrystals reveals a high degree of order indicative of a hexagonally close packed (hcp) superlattice with sharp diffraction peaks prior to ligand exchange (Figure S2, Supporting Information). Using the position of the first GISAXS diffraction peak, we calculate an average center-to-center distance between neighboring nanocrystals equal to 14.9 nm. This agrees with the expected value for two ~13.5 nm diameter nanocrystals hexagonally close packed with oleate ligands that are interdigitated giving a surface-to-surface spacing of ~1.4 nm. After ligand exchange, there is a noticeable loss of medium- to long-range order in the $Cu_{2-x}Se$ films for all ligands used (Figure 2b,d) indicating a random packing of nanocrystals with broad distribution of interparticle spacings. Similar effects have been reported before when using dip coating to build layer-by-layer assemblies of ligand-exchanged nanocrystal thin films.[28] The position of these shoulders is consistent throughout all the samples measured indicating a similar distribution of spacing in all the nanocrystal composite thin films measured. The loss of periodicity and long-range order supports the conclusion that the differences in conductivity and Seebeck coefficients was not the result of packing differences between the nanocrystal films. Instead, surface interactions between the organic ligand and inorganic nanocrystal surface are responsible for our measured results in thermoelectric transport properties.

We also used wide angle XRD on the $Cu_{2-x}Se$ films with symmetric ligands to demonstrate there was no phase change or oxidation state changes during ligand exchange (Figure S3, Supporting Information). It has been shown that the copper chalcogenides' diffraction patterns are especially sensitive to the oxidation states of the copper ions in the crystal lattice. Kriegal *et al.* showed for copper chalcogenides the peak positions of the most intense XRD peaks shift to higher 2θ values as the material transforms from stoichiometric to non-stoichiometric phases through exposure to air.[22] We observe no new peaks or significant shifts in the position of the XRD peaks after ligand exchange, verifying that the measured differences in transport properties (Tables S2 and S3, Supporting Information) were not a result of new crystal phases formed through oxidation. $Cu_{2-x}Se$ nanocrystals and films are characterized by the presence of a broad, intense absorption profile centered in the NIR at 1350 nm attributed to LSPs. After ligand exchange with the symmetric molecules, the LSP shows a tailing off toward longer wavelengths making estimates of any shifts difficult (Figure S3b, Supporting Information). The magnitude of this redshift, where measurable, is negligible and most likely reflects changes to the dielectric environment caused by the different polarities of the surface bound ligands. We took further efforts to confirm that oxygen was not acting as an electron-withdrawing group whereby it could convert Cu(I) to Cu(II) by measuring the XPS spectra of the $Cu_{2-x}Se$–EDT and $Cu_{2-x}Se$–EDA, which have the greatest difference in conductivity among all the samples measured. XPS analysis is well suited to measuring the relative amounts of Cu(I) and Cu(II) on the surface of a material. The presence of satellite peaks at slightly higher binding energies compared to the Cu $2p_{3/2}$ line centered at a binding energy near 932 eV is evidence of the presence of Cu(II) in the material being probed.[29,30] The normalized XPS spectra in Figure S4 (Supporting Information) clearly show near identical spectra for both $Cu_{2-x}Se$–EDT and $Cu_{2-x}Se$–EDA, indicating similar amounts of Cu(I) and Cu(II) in both samples.

We take advantage of the facile charge transport of $Cu_{2-x}Se$ nanocrystal thin films to elucidate ligand effects on transport properties. Highly doped semiconductor nanocrystals allow for small chemical influences among surface ligands to be readily measured as direct differences in conductivity and thermopower. For each ligand, the electrical conductivity, Seebeck coefficient, and calculated power factors are reported in Tables S2 and S3 (Supporting Information). Ligands have a large effect on the transport properties in the resulting $Cu_{2-x}Se$ nanocrystal thin films resulting in conductivity values near 2000 S/cm, a value comparable to that of bulk $Cu_{2-x}Se$.[20] Interestingly, however, even though the electrical conductivity values span 3 orders of magnitude for the different ligands, the measured Seebeck coefficients reside in a much narrower range between 10 and 50 μV/K. Previous reports focusing on 6–8 nm PbSe nanocrystal thin films[25−28] have reported conductivities for different amines (10^{-2}–10^{-3} S/cm), thiol (10^{-5} S/cm), and carboxylic acids (10^{-2}–10^{-4} S/cm) in broad agreement with trends in our measurements reported in Tables S2 and S3 (Supporting Information).

To further explore the role of ligand-coupling symmetry in transport properties, we synthesize a complementary set of $Cu_{2-x}Se$ thin films with nanocrystals coated with asymmetric, single binding group ligands. Here, the ligands can no longer bridge two neighboring nanocrystals leaving the nonpolar side chains of the ligands to interdigitate. The thin films with asymmetric ligands showed significantly smaller conductivities yet showed Seebeck coefficients in the same range of 10–50 μV/K as the symmetric ligands (Figure 4).

To rationalize the strong sensitivity of the conductance and relative insensitivity of S in the measured samples at room temperature shown in Figure 4, we develop a simple explanation due to local interactions between the ligands and nanoparticles. We consider our samples to be a disordered, incoherent 2D network of molecular junctions, where local transport is determined by the probability to coherently tunnel between neighboring nanocrystals. The tunneling probability is controlled by the alignment and coupling of ligand

frontier orbitals relative to the local Fermi level of the nanocrystal. As the films are p-type, the Fermi level lies near the $Cu_{2-x}Se$ valence band edge, and it is assumed that the HOMO resonance energy of the bound ligand determines the effective tunneling barrier height.

Assuming coherent tunneling through the ligand's nondegenerate HOMO, and assuming the HOMO resonance is then positioned at an energy E_0 below the local Fermi energy and is broadened by the sum of its couplings Γ_S and Γ_D to its neighboring source and drain nanocrystals, we can consider the behavior of an energy-dependent tunneling probability, or transmission function [$\tau(E)$], with a Lorentzian line shape possessing a width $\Gamma = \Gamma_S + \Gamma_D$ and peak centered at E_0 (Scheme 1).[31]

Physically, Γ_S and Γ_D are ligand-dependent injection rates for carriers into and out of the molecule. For symmetric ligands, where both ends are chemisorbed: $\Gamma_S \sim \Gamma_D$ with a small variation in coupling throughout the whole film due to the selectivity of the chemical bond. On the other hand, for asymmetric ligands where one end of the ligand is chemisorbed and the other physisorbed to another component in the nanocrystal, we expect $\Gamma_S \gg \Gamma_D$; additionally, while the variation in Γ_S will again be small, similar to that of the symmetric case, variations in Γ_D will be larger as the nonpolar, alkyl chain of the asymmetric ligand is not chemically bound and can couple to other elements in the nanocrystal in a nonselective manner. Using this to understand the relative strengths of the coupling and the variations across the film, we can explore the effect on *S* and *G*. *G* is directly proportional to the transmission function, and *S* is given by its log-derivative (see Scheme 1 and, *e.g.*, Malen *et al.*[9]). Since *G* is proportional to the smallest coupling parameter (or injection rate), Γ_D, the conductance in the asymmetric case is significantly smaller relative to the symmetric case. In contrast, *S* is proportional to E_0, whereas Γ_D enters just additively into the denominator of *S* and is far less sensitive to the symmetry or variation in coupling. This is consistent with experiment, as level alignment (and therefore E_0) is not expected to change dramatically with ligand-binding symmetry or conformation. (Additionally, see Table S1, Supporting Information, where the computed ionization potential does not vary appreciably with symmetry, consistent with a robust E_0.)

The Seebeck coefficients for most of the surface binding group chemistries remain relatively consistent between the symmetric and asymmetric cases, with the exception of 1,2-ethanedithiol where the Seebeck

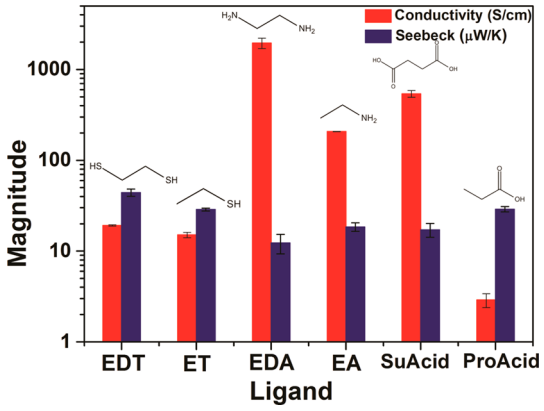

Figure 4. (a) Comparison of conductivity (S/cm) and Seebeck coefficient (μV/K) between symmetric and asymmetric ligands.

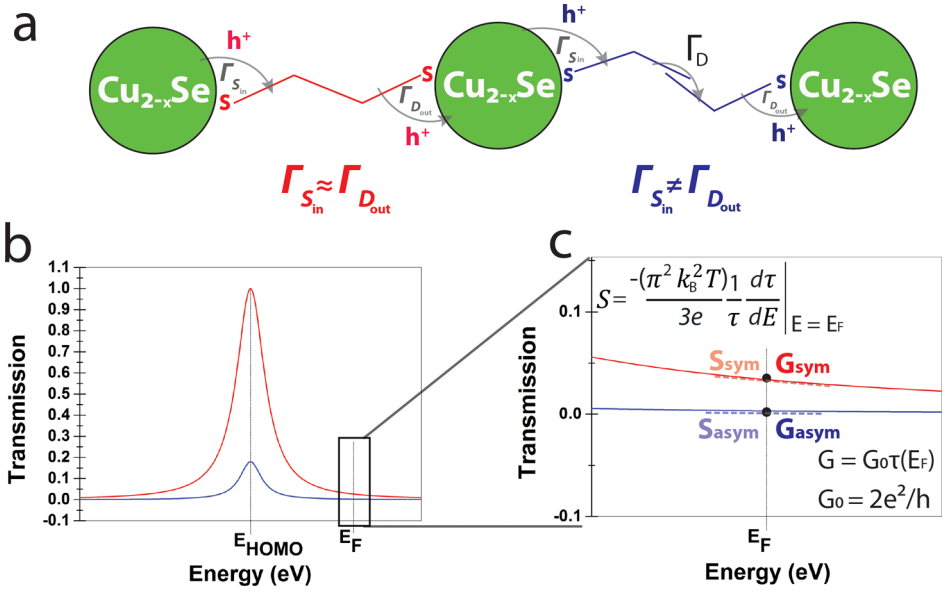

Scheme 1. (a) Three neighboring nanocrystals, on the left bridged by a symmetric ligand and on the right bridged by two asymmetric ligands. (b) A heuristic, representative single-channel, HOMO-dominated transmission function [τ] with a Lorentzian linshape for $\Gamma_S = \Gamma_D$ (red) and $\Gamma_S \gg \Gamma_D$ (blue), plotted analytically for illustrative purposes. (c) Zoom showing a specific level alignment and τ for which conductance (*G*) can differ significantly between symmetric and asymmetric coupling, while thermopower (*S*) need not vary as significantly due to its dependence on the derivative of the natural log of τ at E_F.[31]

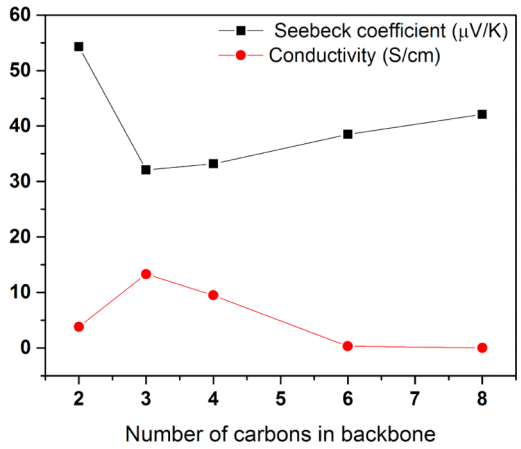

Figure 5. Conductivity and Seebeck coefficient trends as a function of the number of carbon in the backbone of dithiols ligands used in $Cu_{2-x}Se$ thin films.

coefficient decreases approximately 25% along with a similar reduction in conductivity. To rationalize this reduction in both the thermopower and conductivity, we hypothesize that EDT bonds differently than the other ligands to the surface of $Cu_{2-x}Se$ nanocrystals. Luther *et al.* suggested[28] that for PbSe nanocrystals, EDT likely binds in a bidentate mode where both thiol functionalities form bonds to the same nanocrystal surface. The likelihood of such a bonding motif should decrease with the length of the dithiol bond. As the dithiol backbone increases in length, it has to overcome greater numbers of solvent molecules to reach the nanocrystal surface, and it has larger steric hindrances from neighboring ligands limiting its ability to bond in a bidentate fashion. To test the possibility of a characteristic bonding opportunity for EDT, we prepared $Cu_{2-x}Se$ nanocrystal thin films using a series of dithiol ligands with the length of the carbon backbone decreasing (Figure 5). As the length of the dithiol carbon backbone decreases, the measured conductivity increases due to a gradual reduction in interparticle spacing. Theoretically, this effect would manifest itself as an increase of injection rates through the ligand tunneling barrier. However, when the number of carbons in the dithiol backbone is reduced from three to two there is an unexpected decrease in the conductivity from about 13 to 4 S/cm (Figure 5), suggesting a unique binding environment for EDT that does not fit the expected trend.

Another possible explanation of EDT's decrease in conductivity and thermopower when going from symmetric to asymmetric ligands is that it is related to the higher propensity of EDT to dimerize when not chemically protected as compared to amines and carboxylic acids. This dimerization is a consequence of oxidation that can occur during the ligand-exchange process where two dithiol groups can react to form a sulfur–sulfur bond between neighboring nanocrystals. This outcome is more likely in the presence of oxygen, and while all ligand exchanges were performed in an inert atmosphere glovebox, trace oxygen impurities cannot be entirely eliminated and similar observations are known from the surface science and microscopy communities. The three bonding modes affecting transport through EDT are illustrated in Figure S5 (Supporting Information). Further research into the role of the dibinding ligand geometries and length is currently being explored elsewhere and is beyond the scope of the current work.

CONCLUSIONS

We use $Cu_{2-x}Se$ nanocrystals along with commonly used symmetric and asymmetric organic ligands to prepare nanocrystalline composite thermoelectric thin films through careful manipulation of layer-by-layer assembly conditions. We demonstrate how the chemical and physical interfaces present in $Cu_{2-x}Se$ nanocrystal composite thin films controls the thermoelectric transport by discerning clear trends in how the polar binding headgroup and organic linker coupling symmetry affect the electrical conductivity and Seebeck coefficient. We produce near-record power factors for an all nanocrystal inorganic–organic composite of $\sim$30 $\mu W/m \cdot K^2$ and show that organic linker coupling symmetry primarily affects the electrical conductivity while having little impact on the Seebeck coefficient. These observations, partnered with intuition from a microscopic local tunneling picture, provides new physical insight into the processes of charge and energy transport in organic/nanocrystal hybrid materials of interest for thermoelectric energy conversion applications. We envision using these insights to assist in crafting designer energy landscapes for charge and heat to flow through these new classes of materials. Given the relatively profound impact that cross-linking symmetry can have on thermopower; these materials also represent a unique platform for studying how binding symmetries impact thermal transport as well. Given that there is a large thermal impedance mismatch between organic (and inorganic) molecular species and inorganic nanocrystals,[32,33] one might anticipate low thermal conductivity values which further emphasizes the appeal of these materials for thermoelectric energy harvesting.

MATERIALS AND METHODS

Selenium (powder 100 mesh, 99.99%), oleic acid (OA, tech. grade 90%), 1-octadecene (technical grade 90%), copper(I) chloride (99%), oleylamine (OAm, technical grade 70%), anhydrous acetonitrile (ACN, 99.8%), anhydrous methanol (99.8%), anhydrous *N*,*N*-dimethylformaminde (DMF, 99.8%), ethylamine

(EA, 95%), ethylenediamine (EDA, ≥99.5%), propionic acid (≥99.5%), and succinic acid (BioXtra ≥99.0%) were purchased from Aldrich. Triethyloxonium tetrafluoroborate (Et_3OBF_4, 97%) and 1,2 ethanedithiol (EDT, ≥98%), ethanethiol (ET, 97%) were purchased from Fluka. Anhydrous hexanes (DriSolv, >99.8%) and anhydrous ethyl alcohol (200 proof) were purchased from EMD Millipore Chemicals. Bulk hexanes (≥98.5%) and toluene (≥99.5%) were purchased from VWR. All chemicals were used as received.

Synthesis of Copper Selenide ($Cu_{2-x}Se$) Nanocrystals. Copper selenide nanocrystals were synthesized following slightly modified standard procedures under an inert atmosphere.[22] Briefly, selenium powder (94.8 mg, 1.2 mmol) was added to 1-octadecene (9 mL) and OAm (6 mL) in a 50 mL three-necked flask and placed under vacuum at room temperature and 110 °C for 15 min and 1 h, respectively, to dry and de-gas the solution. Afterward, the Se solution was placed under nitrogen flow and raised to 310 °C. The solution was orange and transparent. Separately, in a 25 mL three-necked flask, CuCl (198 mg, 2 mmol), OAm (2 mL), and 1-octadecene (3 mL) were placed under vacuum at 110 °C for 15 min to dry and de-gas the solution. The solution was light green and transparent. Next, the copper solution was rapidly injected into the Se solution, and the reaction temperature dropped to ~285 °C. The reaction temperature was allowed to recover to 300 °C and was kept at this temperature for 20 min. The reaction was cooled in a water bath. The particles were then purified by precipitation three times from hexanes/toluene (50/50 v/v) using ethanol. The particles were suspended in clean hexanes for film deposition.

Fabrication of $Cu_{2-x}Se$ Nanocrystal Films. $Cu_{2-x}Se$ nanocrystalline films were dip coated by hand using a slightly modified layer-by-layer procedure described in detail elsewhere.[28] The substrates, rectangular glass slides, or double-side-polished i-Si(100) wafers, cleaned by sonication in acetone and 2-propanol for 10 min, then rinsed in clean 2-propanol) were dipped into a ~5 mg/mL solution of $Cu_{2-x}Se$ nanocrystals in dry hexane at a rate of ~0.5 cm/s and then in solution of EDT in dry ACN (0.1 M) for 10 s, EDA in dry methanol (1.0 M) for 1 min, succinic acid in dry ACN (0.1 M) for 1 min, or for ligand stripping, Et_3OBF_4 in a 9:1 v/v dry ACN/DMF (20 mM) for 35 s. Similar exchange concentrations and times are used for asymmetric, monofunctional ligands with the same binding group. After ligand exchange, the films were rinsed with dry ACN or methanol followed by dry hexanes to remove excess ligands. To ensure near complete ligand exchange and thorough rinsing of excess ligands, films were prepared with thicknesses of 65−80 nm for conductivity and Seebeck measurements. To maximize signal intensity, ~200 nm thick films were prepared for IR, XRD, and GISAXS measurements.

Characterization. SEM images were recorded on a Zeiss Gemini Ultra-55 analytical scanning electron microscope using beam energy of 5 kV and an In-Lens detector. TEM images were recorded on an Analytical JEOL-2100F FETEM using beam energy of 200 kV, equipped with a Gatan camera. Wide-angle XRD was performed on a Bruker Gadds-8 diffractometer with a Cu Kα source operating at 40 kV and 20 mA. FT-IR spectra were obtained using a Perkin Elmer Spectrum One FT-IR spectrometer on double-side polished Si substrates.

X-ray Photoelectron Spectroscopy. XPS surface analysis was performed using a PHI 5400 XPS analyzer. The XPS analysis was performed in ultrahigh vacuum (UHV) conditions, with the electron analyzer at 45° to the sample surface normal and the Al K_α X-ray source (1486.6 eV) at 54.4° relative to the electron analyzer with an approximate escape depth of 5 nm.

Grazing Incidence Small-Angle X-ray Scattering (GISAXS) Measurements. GISAXS was done at the beamline 12-ID-B of the Advanced Photon Source at the Argonne National Laboratory. The incident angles of the 14 keV (0.886 Å) X-ray beam ranged from 0.02 to 0.15°, where the critical angle of the silicon substrate is about 0.127° at the energy. The scattered photons from 1-s exposures were collected using a Pilatus 2 M area detector positioned at 2029.4 mm from the sample (the detector was relocated to 3639.6 mm to access to smaller q region). The standard used for *q* calibration was silver behenate. Data reduction was performed using computer program GISAXShop available at the beamline to make horizontal linecuts along q_xy.

Electrical Conductivity and Seebeck Coefficient Measurements. Electrical conductivity was measured using a Keithley 2400 sourcemeter in a four-wire Van der Pauw configuration. For conductivity and Seebeck measurements, four 100 nm thick gold contacts were deposited near the corners of the dip-coated film *via* thermal evaporation. Thermopower (Seebeck coefficient) was measured using a homemade setup consisting of two Peltier devices (Ferrotec) spaced ~4 mm apart. Current was driven through the devices in opposing polarities, resulting in a temperature gradient about room temperature which varied with the magnitude of the current. The temperature of the sample was measured using two T-type thermocouples mounted in micromanipulators. Thermal contact was ensured by utilizing silicon thermal paste (Wakefield Thermal Solutions). Typically, five different thermal gradients were employed, with 10 voltage samples taken and averaged using an Agilent 34401 multimeter. The value of V_{oc} was linear with ΔT for all of the films within the temperature range measured. For each organic ligand used, three samples were prepared to measure conductivity and Seebeck coefficient.

Functional Form of Lorentzian Model. The conductance and thermopower power are given by the following expression when the transmission has a Lorentzian line shape with width $\Gamma = \Gamma_S + \Gamma_D$ and peak centered at E_0 below the Fermi energy E_F

$$G = \frac{2e^2}{h}\frac{\Gamma_S\Gamma_D}{\frac{1}{4}(\Gamma_S+\Gamma_D)^2 + (E_F - E_0)^2} \quad (2)$$

$$S = \frac{2}{3}\frac{\pi^2 k_B^2 T}{e}\frac{E_F - E_0}{\frac{1}{4}(\Gamma_S+\Gamma_D)^2 + (E_F - E_0)^2} \quad (3)$$

where k_B is Boltzmann's constant, e is the electronic charge, and T is the average temperature.[31]

Conflict of Interest: The authors declare no competing financial interest.

Supporting Information Available: SEMs of $Cu_{2-x}Se$ composite thin films with asymmetric ligands, wide-angle XRD, and absorption spectra of $Cu_{2-x}Se$ composite thin films with symmetric ligands, XPS spectra of $Cu_{2-x}Se$EDA and EDT, UPS spectra of $Cu_{2-x}Se$ composite thin films with symmetric ligands, dithiol binding modes, table of ionization potentials, tables of exact values of all transport measurements, and transport scheme. This material is available free of charge *via* the Internet at http://pubs.acs.org.

Acknowledgment. This work is supported by AFOSR MURI FA9550-12-1-0002. Portions of this work were done at the Molecular Foundry, supported by the Office of Science, Office of Basic Energy Sciences, of the U.S. Department of Energy under Contract No. DE-AC02-05CH11231. Use of the Advanced Photon Source, an Office of Science User Facility operated for the U.S. Department of Energy (DOE) Office of Science by Argonne National Laboratory, was supported by the U.S. DOE under Contract No. DE-AC02-06CH11357 and supported by NSF MRSEC DMR-0520020. We acknowledge Dr. Nelson Coates for his thoughtful insight and helpful discussion of the transport properties in our composite systems. We alsoacknowledge Amy Bergerud for her assistance in measuring XPS spectra of our composite thin films.

REFERENCES AND NOTES

1. Cadavid, D.; Ibanez, M.; Gorsse, S.; Lopez, A. M.; Cirera, A.; Morante, J. R.; Cabot, A. Bottom-Up Processing of Thermoelectric Nanocomposites from Colloidal Nanocrystal Building Blocks: The Case of Ag_2Te-PbTe. *J. Nanopart. Res.* **2012**, *14*, 1–10.
2. Hanrath, T. Colloidal Nanocrystal Quantum Dot Assemblies as Artificial Solids. *J. Vac. Sci. Technol., A* **2012**, *30* (030802), 1–28.
3. Cadavid, D.; Ibanez, M.; Shavel, A.; Dura, O. J.; de la Torre, M. A. L.; Cabot, A. Organic Ligand Displacement by Metal

Salts to Enhance Nanoparticle Functionality: Thermoelectric Properties of Ag_2Te. *J. Mater. Chem. A* **2013**, *1*, 4864–4870.
4. Pichanusakorn, P.; Bandaru, P. Nanostructured Thermoelectrics. *Mater. Sci. Eng., R* **2010**, *67*, 19–63.
5. Wang, R. Y.; Feser, J. P.; Lee, J. S.; Talapin, D. V.; Segalman, R.; Majumdar, A. Enhanced Thermopower in PbSe Nanocrystal Quantum Dot Superlattices. *Nano Lett.* **2008**, *8*, 2283–2288.
6. Vineis, C. J.; Shakouri, A.; Majumdar, A.; Kanatzidis, M. G. Nanostructured Thermoelectrics: Big Efficiency Gains from Small Features. *Adv. Mater.* **2010**, *22*, 3970–3980.
7. Androulakis, J.; Lin, C.-H.; Kong, H.-J.; Uher, C.; Wu, C.-I.; Hogan, T.; Cook, B. A.; Caillat, T.; Paraskevopoulos, K. M.; Kanatzidis, M. G. Spinodal Decomposition and Nucleation and Growth as a Means to Bulk Nanostructured Thermoelectrics: Enhanced Performance in $Pb_{1-x}Sn_xTe$-PbS. *J. Am. Chem. Soc.* **2007**, *129*, 9780–9788.
8. Uchida, N.; Tada, T.; Ohishi, Y.; Miyazaki, Y.; Kurosaki, K.; Yamanaka, S. Heavily Doped Silicon and Nickel Silicide Nanocrystal Composite Films with Enhanced Thermoelectric Efficiency. *J. Appl. Phys.* **2013**, *114* (134311), 1–6.
9. Malen, J. A.; Yee, S. K.; Majumdar, A.; Segalman, R. A. Fundamentals of Energy Transport, Energy Conversion, and Thermal Properties in Organic-Inorganic Heterojunctions. *Chem. Phys. Lett.* **2010**, *491*, 109–122.
10. Reddy, P.; Jang, S. Y.; Segalman, R. A.; Majumdar, A. Thermoelectricity in Molecular Junctions. *Science* **2007**, *315*, 1568–1571.
11. Muller, K. H. Thermoelectrics in an array of molecular junctions. *J. Chem. Phys.* **2008**, *129* (044708), 1–11.
12. Kato, K.; Hagino, H.; Miyazaki, K. Fabrication of Bismuth Telluride Thermoelectric Films Containing Conductive Polymers Using a Printing Method. *J. Electron. Mater.* **2013**, *42*, 1313–1318.
13. Baheti, K.; Malen, J. A.; Doak, P.; Reddy, P.; Jang, S.-Y.; Tilley, T. D.; Majumdar, A.; Segalman, R. A. Probing the Chemistry of Molecular Heterojunctions Using Thermoelectricity. *Nano Lett.* **2008**, *8*, 715–719.
14. Malen, J. A.; Doak, P.; Baheti, K.; Tilley, T. D.; Segalman, R. A.; Majumdar, A. Identifying the Length Dependence of Orbital Alignment and Contact Coupling in Molecular Heterojunctions. *Nano Lett.* **2009**, *9*, 1164–1169.
15. Nitzan, A.; Ratner, M. A. Electron Transport in Molecular Wire Junctions. *Science* **2003**, *300*, 1384–1389.
16. Batra, A.; Darancet, P.; Chen, Q.; Meisner, J. S.; Widawsky, J. R.; Neaton, J. B.; Nuckolls, C.; Venkataraman, L. Tuning Rectification in Single-Molecular Diodes. *Nano Lett.* **2013**, *13*, 6233–6237.
17. Rowe, D. M.; Gao, M. Multiple Potential Barriers as a Possible Mechanism to Increase the Seebeck Coefficient and Electrical Power Factor. *AIP Conf. Proc.* **1995**, *316*, 339–342.
18. Vashaee, D.; Shakouri, A. Electronic and Thermoelectric Transport in Semiconductor and Metallic Superlattices. *J. Appl. Phys.* **2004**, *95*, 1233–1245.
19. Brown, D. R.; Day, T.; Borup, K. A.; Christensen, S.; Iverson, B. B.; Snyder, G. J. Phase Transition Enhanced Thermoelectric Figure-of-Merit in Copper Chalcogenides. *APL Mater.* **2013**, *1* (052107), 1–10.
20. Liu, H.; Shi, X.; Xu, F.; Zhang, L.; Zhang, W.; Chen, L.; Li, Q.; Uher, C.; Day, T.; Snyder, G. J. Copper Ion Liquid-Like Thermoelectrics. *Nat. Mater.* **2012**, *11*, 422–425.
21. Riha, S. C.; Johnson, D. C.; Prieto, A. L. Cu_2Se Nanoparticles with Tunable Electronic Properties Due to a Controlled Solid-State Phase Transition Driven by Copper Oxidation and Cationic Conduction. *J. Am. Chem. Soc.* **2011**, *133*, 1383–1390.
22. Kriegel, I.; Jiang, C.; Rodriguez-Fernandez, J.; Schaller, R. D.; Talapin, D. V.; da Como, E.; Feldmann, J. Tuning the Excitonic and Plasmonic Properties of Copper Chalcogenide Nanocrystals. *J. Am. Chem. Soc.* **2012**, *134*, 1583–1590.
23. Luther, J. M.; Jain, P. K.; Ewers, T.; Alivisatos, A. P. Localized Surface Plasmon Resonances Arising from Free Carriers in Doped Quantum Dots. *Nat. Mater.* **2011**, *10*, 361–366.
24. Mendelsberg, R. J.; Garcia, G.; Li, H.; Manna, L.; Milliron, D. J. Understanding the Plasmon Resonance in Ensembles of Degenerately Doped Semiconductor Nanocrystals. *J. Phys. Chem. C* **2012**, *116*, 12226–12231.
25. Rosen, E. L.; Buonsanti, R.; Llordes, A.; Sawvel, A. M.; Milliron, D. J.; Helms, B. A. Exceptionally Mild Reactive Stripping of Native Ligands from Nanocrystal Surfaces by Using Meerwein's Salt. *Angew. Chem., Int. Ed.* **2012**, *51*, 684–689.
26. Law, M.; Luther, J. M.; Song, O.; Hughes, B. K.; Perkins, C. L.; Nozik, A. J. Structural, Optical, and Electrical Properties of PbSe Nanocrystal Solids Treated Thermally or with Simple Amines. *J. Am. Chem. Soc.* **2008**, *130*, 5974–5985.
27. Zarghami, M. H.; Liu, Y.; Gibbs, M.; Gebremichael, E.; Webster, C.; Law, M. p-Type PbSe and PbS Quantum Dot Solids Prepared with Short-Chain Acids and Diacids. *ACS Nano* **2010**, *4*, 2475–2485.
28. Luther, J. M.; Law, M.; Song, Q.; Perkins, C. L.; Beard, M. C.; Nozik, A. J. Structural, Optical and Electrical Properties of Self-Assembled Films of PbSe Nanocrystals Treated with 1,2-ethanedithiol. *ACS Nano* **2008**, *2*, 271–280.
29. Biesinger, M. C.; Hart, B. R.; Polack, R.; Kobe, B. A.; Smart, R. S. C. Analysis of Mineral Surface Chemistry in Flotation Separation Using Imaging XPS. *Miner. Eng.* **2007**, *20*, 152–162.
30. Biesinger, M. C.; Lau, L. W. M.; Gerson, A. R.; Smart, R. S. C. Resolving Surface Chemical States in XPS analysis of First Row Transition Metals, Oxides and Hydroxides: Sc, Ti, V, Cu and Zn. *Appl. Surf. Sci.* **2010**, *257*, 887–898.
31. Paulsson, M.; Datta, S. Thermoelectric effect in molecular electronics. *Phys. Rev. B* **2003**, *67* (241403), 1–4.
32. Ong, W. L.; Rupich, S. M.; Talapin, D. V.; McGaughey, A. J. H.; Malen, J. A. Surface Chemistry Mediates Thermal Transport in Three-Dimensional Nanocrystal Arrays. *Nat. Mater.* **2013**, *12*, 410–415.
33. Feser, J. P.; Chan, E. M.; Majumdar, A.; Segalman, R. A.; Urban, J. J. Ultralow Thermal Conductivity in Polycrystalline CdSe Thin Films with Controlled Grain Size. *Nano Lett.* **2013**, *13*, 2122–2127.